Front contact optimization for rear-junction SHJ solar cells with ultra-thin n-type nanocrystalline silicon oxide

Depeng Qiu, Weiyuan Duan*, Andreas Lambertz, Karsten Bittkau, Paul Steuter, Yong Liu, Alaaeldin Gad, Manuel Pomaska, Uwe Rau, Kaining Ding

IEK-5 Photovoltaik, Forschungszentrum Jülich, 52425 Jülich, Germany

Abstract

In this work, ultra-thin n-type hydrogenated nanocrystalline silicon oxide ((n) nc-SiO_x:H) film was used to replace amorphous silicon ((n) a-Si:H) as electron transport layer (ETL) in rear-junction silicon heterojunction (SHJ) solar cell to reduce front parasitic absorption. The contact resistivity between the transparent conductive oxide (TCO) and ultra-thin ETL interface plays an important role on the cell performance. A nanocrystalline silicon (nc-Si:H) contact or seed layer was introduced in solar cell with ultra-thin nc-SiO_x:H and the impact of the nc-Si:H thickness on the cell performance was investigated. Lower front contact resistivity can be obtained by replacing nc-SiO_x:H layer with nc-Si:H/nc-SiO_x:H double layer or increasing the thickness of ETL, which is caused by the lower energy barrier for electrons, according to the band diagram calculated by the AFORS-HET simulator. For solar cell with 10 nm double layer, an increase of 0.4 mA/cm^2 of short-circuit current density (J_{sc}) and 0.3%$_{abs}$ of fill factor (*FF*) is demonstrated, compared with solar cell with 20 nm nc-SiO_x:H single layer. A solar cell with 5nm nc-SiOx:H and 5nm nc-Si:H contact layer exhibits open-circuit voltage (V_{oc}) of 726 mV, *FF* of 78.6%, J_{sc} of 39.6 mA/cm^2 and power conversion efficiency (η) of 22.6% with an aperture area of 19×19 mm^2. To demonstrate scalability, bifacial solar cells were fabricated on the M2 (244 cm^2) wafer and η of 23.1% is achieved, the optical and electrical losses of which were analyzed by the Quokka 3 simulator. The simulation shows much lower electrical transport losses for solar cells with double layer and a bit higher optical losses, compared with the one with nc-SiO_x:H single layer.

Keywords: Silicon heterojunction solar cells; Nanocrystalline silicon oxide; Loss analysis; Electron transport layer;

* Corresponding author.
Email address: w.duan@fz-juelich.de

1. Introduction

The silicon heterojunction (SHJ) solar cells draw extensive attention and have progressed rapidly over the past few years due to their high efficiencies, low temperature processes and better temperature coefficient compared to conventional crystalline solar cells [1-12]. The SHJ solar cells with two side contact have demonstrated a record conversion efficiency of 25.11% for M2 (244 cm^2) size device by Hanergy [3]. For standard SHJ solar cells, the hydrogenated doped amorphous silicon (a-Si:H) is usually used for carrier-selective layers and transparent conductive oxide (TCO) are placed upon the doped a-Si:H layer as front contact and anti-reflective layers on both sides.

Although the doped a-Si:H window layer is only a few nanometers thick (5 - 10 nm), it still absorbs a significant amount of incoming light parasitically, which leads to a reduction of the short-circuit current density (J_{sc}) of 1.6 mA/cm^2 for the solar cells [13, 14]. Besides, the reflection at the TCO (refractive index at 632 nm, n~2.0) / silicon (n~3.8) interface is increased by the a-Si:H stacks (n~4.0) [15, 16]. To reduce the parasitic absorption and the reflection, hydrogenated nanocrystalline silicon oxide (nc-SiO_x:H) has been proved to be a highly promising alternative to the commonly used doped a-Si:H [16-23]. The nc-SiO_x:H is a two-phase material with nanocrystalline silicon (nc-Si) that has higher doping efficiency than a-Si:H, embedded in a highly transparent amorphous silicon oxide (a-SiO_x) matrix [23-25]. Compared with a-Si:H films, the nc-SiO_x:H films have following advantages: i) higher optical transparency, meantime with similar electrical conductivity and ii) lower refractive index [16, 26]. Therefore, replacing a-Si:H with nc-SiO_x:H as window layer in solar cells is a promising candidate to achieve higher J_{sc} [26].

However, the crystalline growth of the nc-SiO_x:H layer is substrate selective and starts after a certain amorphous incubation layer with an intrinsic a-Si:H ((i) a-Si:H) layer underneath [27-30]. Therefore, the preparation of ultra-thin nc-SiO_x:H layers with a sufficient crystalline volume fraction on top of the (i) a-Si:H layer and without a deterioration of the passivation is a big challenge for SHJ solar cells. Depositing the nc-SiO_x:H on a nc-Si:H seed layer has been suggested to induce a fast nucleation of crystallites, thereby resulting in an ultra-thin nc-SiO_x:H

layers with a higher crystalline volume fraction in SHJ solar cells [21, 31-33]. Besides, S. Kirner et al found that the contact property of TCO and p-type nc-SiO_x:H has a big influence on solar cell performance and can be improved by inserting a p-type nc-Si:H contact layer between TCO and p-type nc-SiO_x:H layers [15]. L. Mazzarella et al applied n-type nc-Si:H contact or seed layer in solar cell with nc-SiO_x:H of varied thickness, but the impacts of the n-type nc-Si:H seed and contact layer thickness on the cell performance was not mentioned [21].

In this paper, ultra-thin n-type nc-SiO_x:H layers were prepared in a low-pressure-low-power plasma enhanced chemical vapor deposition (PECVD) system and applied as ETL in rear-junction SHJ solar cells. The nc-Si:H contact and seed layer of different thicknesses were used to optimize the front contact properties. To investigate the principle of introducing contact or seed layer, the energy band diagrams of the solar cells were simulated by the device simulator, AFORS-HET [34, 35]. Additionally, the process was transferred to M2 size solar cells with smart wire to demonstrate the feasibility on larger area. The main loss mechanisms of device on M2 size wafer was identified and simulated by the commercial device simulator, Quokka 3 [36-38].

2. Experiment method

The nc-Si:H and nc-SiO_x:H films described in this study were deposited by PECVD at 13.56 MHz plasma excitation frequency, 80 mW/cm^2 power density, 2.5 mbar deposition pressure and a heater temperature of 200°C. For (n) nc-Si:H film the precursor gases we used are SiH_4, H_2 and PH_3, while CO_2 was additionally added and the gas flow of SiH_4, H_2 and PH_3 was same as (n) nc-Si:H film during the deposition of n-type nc-SiO_x:H. For material development, the silicon films with thicknesses of 40-50 nm were deposited on glasses (Corning Eagle 2000).

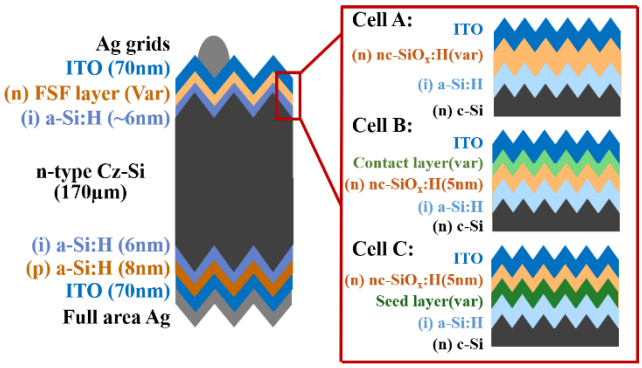

Fig. 1. Schematic cross-section of rear-junction SHJ solar cell structures with three different electron transport layer (ETL) stacks: Cell A with nc-SiO_x:H single layer, cell B with contact layer and 5nm nc-SiO_x:H, and cell C with seed layer and 5nm nc-SiO_x:H. Both contact and seed layer are n-type nc-Si:H films.

The structures of the devices in this paper are shown in Fig. 1. Cell A has an ETL consisting of an n-type nc-SiO_x:H single layer, thickness of which was varied from 5 to 20 nm. Cell B and C has an ETL stack consisting of a double layer (n-type nc-SiO_x:H and nc-Si:H contact or seed layer), where the nc-SiO_x:H film was fixed at 5 nm and the nc-Si:H thickness was varied from 0 to 10 nm.

The rear-junction SHJ solar cells have a designated area of four 19 × 19 mm^2 cells distributed on a 78 × 78 mm^2 wafer. We used textured n-type Czochralski silicon wafers with thickness of 170 µm, size of 78 × 78 mm^2 and resistivity of 2-5 Ω cm. Before PECVD depositions, the wafers were cleaned by an Ozone cleaning procedure and dipped in 1% HF. Afterwards, the front and rear side silicon stacks were grown separately in two chambers. Quasi-steady-state photo-conductance (QSSPC) lifetime measurement was followed immediately, from which the implied V_{oc} (iV_{oc}) can be extracted. Subsequently, 70 nm indium tin oxide (ITO) layers were deposited through a shadow mask on each side at a substrate temperature of 200°C by direct current sputtering. A full area Ag layer for the individual cells on the rear side and an Ag grid on the illuminated side were screen printed, afterwards the samples were annealed at 190°C for 40 minutes.

To evaluate the performance of cells, the current-voltage characteristics under standard test conditions (1.5 AM, 25°C and 100 mW/cm^2) and the external quantum efficiency (EQE) were measured by the LOANA solar cell analysis system from pv-tools with a Wavelabs Sinus 220 light sources. To calculate the pseudo-*FF* (*pFF*) of the solar cell, the J_{sc}-V_{oc} curve was also measured by the LOANA solar cell analysis system. To determine the contact resistance of the

cells, the transfer-length-method (TLM) contact pad arrays were used, which were made by sputtering ITO and screen-printing Ag through a shadow mask on the same wafer beside the cells.

3. Result and discussion

The opto-electrical properties of the nc-SiO_x:H were varied and optimized by the gas flow during PECVD process. The nc-SiO_x:H material was optimized with respect to a high band gap and a sufficient conductivity for solar cell applications and has the following properties at thicknesses of 40-50 nm on glass: a co-planar conductivity (σ) of 0.02 S/cm, a crystalline volume fraction (F_c) of 23% determined by Raman spectroscopy, a refractive index (n) of 2.82 at 632nm determined by Ellipsometry measurement and an optical band gap (E_{04}) of 2.24 eV determined by using a UV-VIS spectrophotometer. For nc-Si:H layers, the σ, F_c, n and E_{04} are 23.1 S/cm, 46%, 3.81 and 1.98 eV, respectively.

3.1 Solar cell results

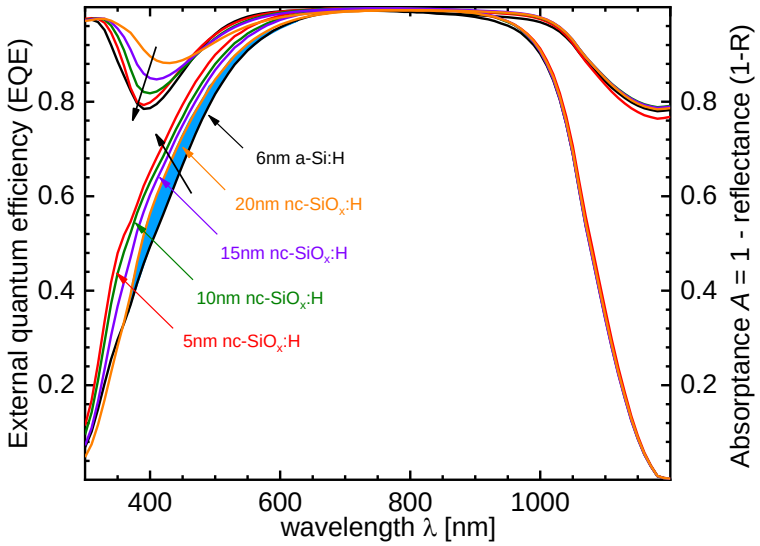

Fig. 2. External quantum efficiency (EQE) and 1-reflection (1-R) spectra as a function of wavelength for the cells with various thickness of (n) nc-SiOx:H film.

Fig. 2 shows the external quantum efficiency (EQE) and absorptance (A) as a function of wavelength for the cells with 7 nm (n) a-Si:H and (n) nc-SiO_x:H layers with different thicknesses. Solar cells with nc-SiO_x:H show a higher *EQE* in the wavelength range from 300 nm to 600 nm as solar cells with n-type a-Si:H. The EQE for solar cells with thinner nc-SiO_x:H layers increase as expected due to a reduced parasitic absorption. Additionally, the

absorptance decreases for thinner nc-SiO$_x$:H layers as a consequence of the increase in reflection, this is an additional chance to further increase the J_{sc} by tuning the anti-reflection coating thickness in further investigations.

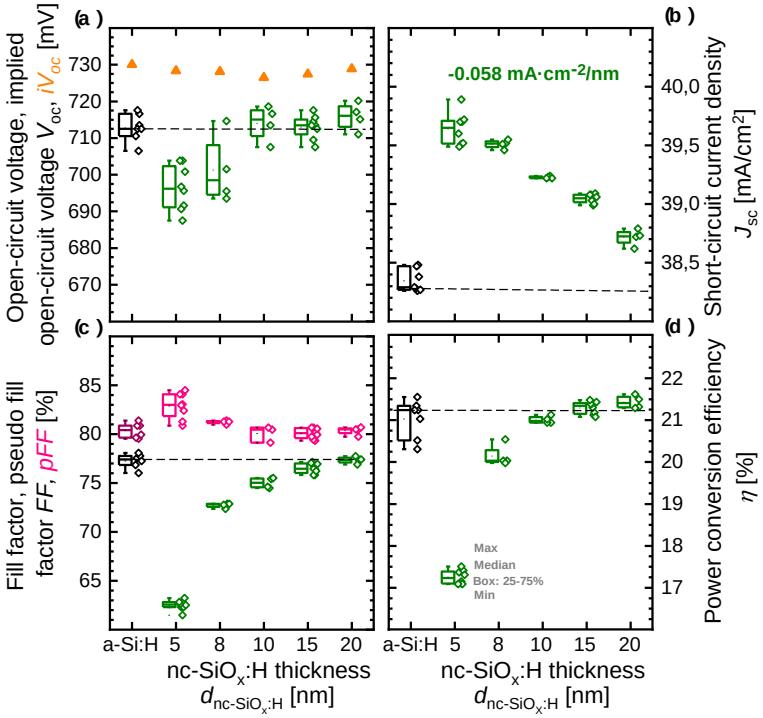

Fig. 3. Box plot of (a) open-circuit voltage (V_{oc}) and implied V_{oc} (iV_{oc}), (b) short-circuit current density (J_{sc}), (c) pseudo fill factor and fill factor (pFF, FF), and (d) power conversion efficiency (η) versus the thickness of the nc-SiOx:H layer ($d_{nc\text{-}SiOx:H}$) for cells with (n) nc-SiO$_x$:H single layer (cell A). The box plots summarize the statistic of 8-10 cells per group. The inner box is the area between the upper, lower quartiles and includes the median. The cell with (n) a-Si:H film is used as reference on the left side.

The IV - parameters of the solar cells with different thicknesses of nc-SiO$_x$:H single layer ($d_{nc\text{-}SiOx:H}$) are shown in Fig. 3. The box plot summarizes the statistic of 8-10 cells per group. The cell with 7nm (n) a-Si:H ETL is used as reference for this series. When decreasing $d_{nc\text{-}SiOx:H}$ from 20 to 10 nm the V_{oc} of the cells is unaffected, but it decreases for (n) nc-SiO$_x$:H layers below 10 nm. The iV_{oc} of the cells with nc-SiO$_x$:H layer of different thicknesses are on the same level as reference cell. Fig. 3(b) shows that J_{sc} increases with decreasing $d_{nc\text{-}SiOx:H}$ by -0.058 mA·cm^{-2}/nm and the gain of J_{sc} is 0.4 – 1.4 mA/cm^2 compared with the reference cell. Fig. 3(c) shows that FF decreases with reducing $d_{nc\text{-}SiOx:H}$ and is more sensitive to $d_{nc\text{-}SiOx:H}$ when it is below 10 nm. Furthermore, there is an increase of the difference between pFF and FF which indicates an increase of the series resistance (R_s) when reducing the $d_{nc\text{-}SiOx:H}$. Although the

power conversion efficiency η of the solar cell with 5 nm nc-SiO_x:H layer is lower than others (Fig. 3(d)), a high J_{sc} of 39.9 mA/cm^2 and similar iV_{oc} as the reference cell can be obtained, which indicates a potential to reach high efficiency assuming a low series resistance.

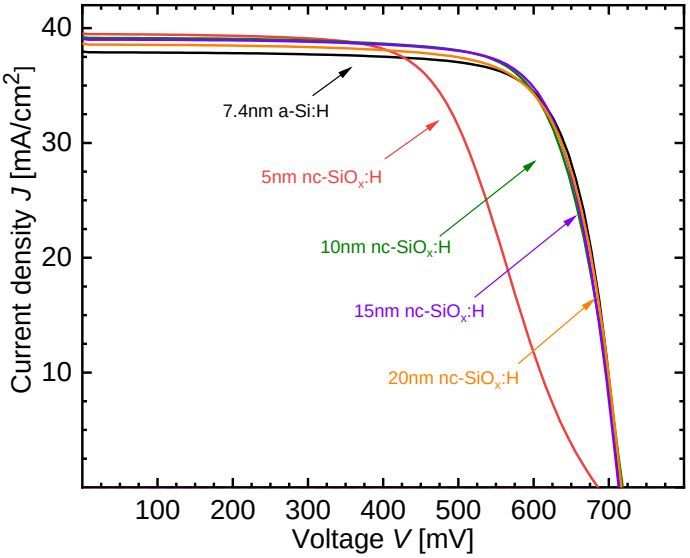

Fig. 4. *J-V* curve of the cells with different thickness of nc-SiO_x:H film on the front side.

Fig. 4 shows the current density as a function of the voltage (*J-V* curve) of the solar cells with 7nm n) a-Si:H and (n) nc-SiO_x:H layers with different thicknesses. The solar cell with 5 nm (n) nc-SiO_x:H has a s-shaped *J-V* curve resulting in a low *FF* and a low V_{oc}, which cannot be observed for the solar cells with thicker (n) nc-SiO_x:H layers. The s-shaped *J-V* curve for solar cell with 5 nm (n) nc-SiO_x:H layer might be related to an electrical transport barrier on the front side, which suggests that the contact resistance of ITO / (n) nc-SiO_x:H interface plays a big role on the cell performance for solar cells with ultra-thin ETL. In order to increase *FF* but keep high J_{sc}, the cell B structure with nc-Si:H contact layer was introduced to optimize the electrical properties of ITO / ETL interface. The box plot of cell performance of cell B versus the thickness of nc-Si:H contact layer ($d_{contact}$) can be seen in Fig. 5.

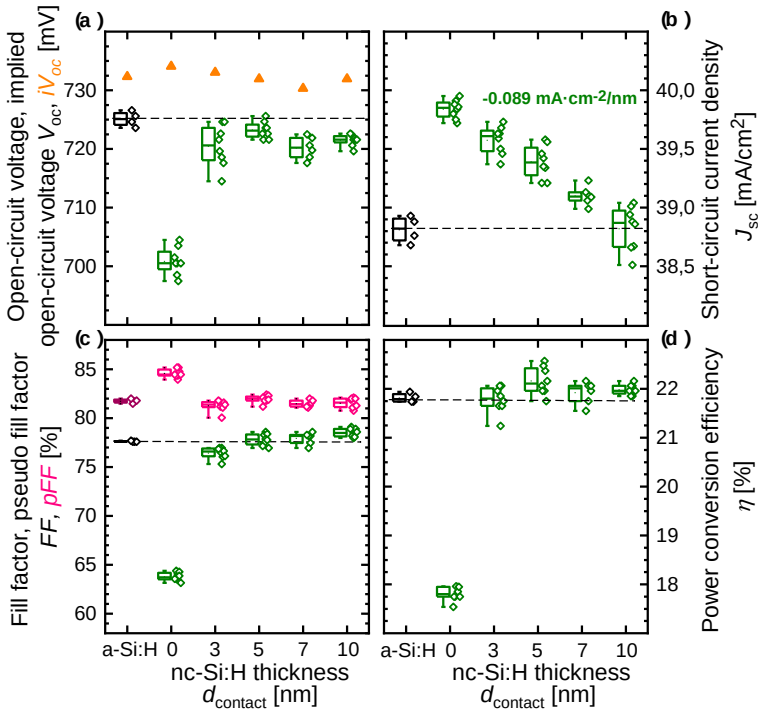

Fig. 5. Box plot of (a) open circuit voltage (V_{oc}) and implied V_{oc} (iV_{oc}), (b) short circuit current density (J_{sc}), (c) pseudo fill factor and fill factor (*pFF, FF*), and (d) power conversion efficiency (η) versus the thickness of the contact layer ($d_{contact}$) for cell structure with contact layer (cell B). The nc-SiO_x:H film was fixed at 5 nm and the nc-Si:H thickness was varied from 0 to 10 nm. The box plots summarize the statistic of 8-10 cells per group. The inner box is the area between the upper, lower quartiles and includes the median. The cell with (n) a-Si:H film is used as reference on the left side.

Fig. 5(a) indicates that the iV_{oc} of the solar cells is similar as reference cell and unaffected by $d_{contact}$. As shown in Fig. 5(b), the J_{sc} of the solar cell decreases with increasing $d_{contact}$ by 0.089 mA·cm^{-2}/nm. Fig. 5(c) shows that the $d_{contact}$ has a big influence on *FF* when it is below 3 nm. The solar cells with more than 5 nm contact layer have a similar fill factor as reference cell. The solar cell with 5 nm contact layer shows the highest power conversion efficiency in this series and exhibits η of 22.6%, V_{oc} of 726 mV, *FF* of 78.6% and J_{sc} of 39.6 mA/cm^2, meantime 0.8 mA/cm^2 gain of J_{sc} compared with the reference cell with n-type a-Si:H layer.

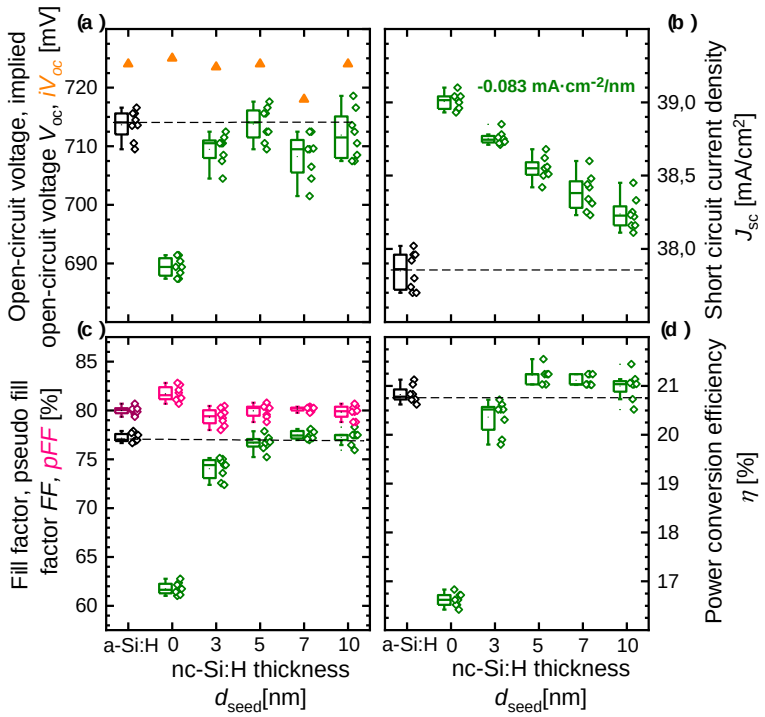

Fig. 6. Box plot of (a) Open circuit voltage (V_{oc}) and implied V_{oc} (iV_{oc}), (b) short circuit current density (J_{sc}), (c) pseudo fill factor and fill factor (pFF, FF), and (d) power conversion efficiency (η) versus the thickness of the seed layer (d_{seed}) for cell structure with seed layer (cell C). The nc-SiO$_x$:H film was fixed at 5 nm and the nc-Si:H thickness was varied from 0 to 10 nm. The box plots summarize the statistic of 8-10 cells per group. The inner box is the area between the upper, lower quartiles and includes the median. The cell with (n) a-Si:H film is used as reference on the left side.

During the deposition process of nc-SiO$_x$:H layer, a certain amorphous phase appears firstly as the nucleation of crystalline phase, then the epitaxial growth is followed [28-31]. Therefore, another way to increase the crystalline volume fraction at the nc-SiO$_x$:H / ITO interface is use of a nc-Si:H seed layer between (i) a-Si:H and nc-SiO$_x$:H layer to induce fast nucleation of crystalline phase. In the cell C structure, a nc-Si:H seed layer was used to support the crystalline growth of the nc-SiO$_x$:H layer. The cell performance as a function of seed layer thickness (d_{seed}) is shown in Fig. 6. Solar cells with seed layers show similar V_{oc} and iV_{oc} as the reference cell with (n) a-Si:H layer and the J_{sc} decreases as increasing d_{seed} by 0.083 mA·cm^{-2}/nm. Fig. 6(c) demonstrates that the FF of the solar cell is more sensitive to d_{seed} when it is below 3 nm. The solar cell with 5 nm seed layer achieves best cell performance in this series and reached 21.5% power conversion efficiency, with a 0.7 mA/cm^2 gain of J_{sc} compared with reference cell. Due to cleaning problem, thicker ITO (80nm) layer and worse wafer quality, this batch shows a

worse performance which can be seen from reference cell compared with cell B series.

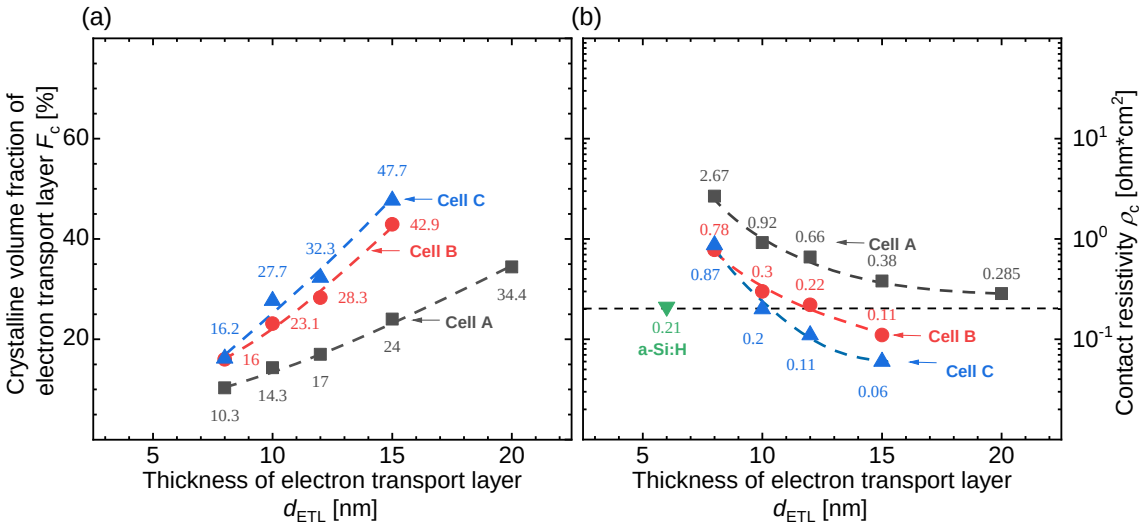

Fig. 7. The crystalline volume fraction (F_c) of the ETL determined by UV-Raman spectroscopy and contact resistivity extracted from transfer-length-method (TLM) measurement as a function of the thickness of electron transport layer (ETL) for cell structure with nc-SiO$_x$:H single layer (cell A), with contact layer and 5 nm nc-SiO$_x$:H (cell B, varying nc-Si:H contact layer thickness), and with seed layer and 5 nm nc-SiO$_x$:H (cell C, varying nc-Si:H seed layer thickness). The cell structure is depicted in Fig. 1.

Fig. 7 shows the crystalline volume fraction (F_c) of ETL and the front contact resistivity versus the total ETL thickness (d_{ETL}) of the solar cells with three different ETLs. The F_c of ETL increases with increasing the thickness and more crystalline ETL can be obtained at the same thickness for the ETL with nc-Si:H contact or seed layer compared with nc-SiO$_x$:H single layer. The front contact of the solar cells with 5 nm ETL (5 nm nc-SiO$_x$:H single layer) is non-ohmic, the contact resistivity (ρ_c) of which is too high to extract accurate value by TLM. The ρ_c of cell A increase when decreasing the thickness of nc-SiO$_x$:H from 20 nm to 8 nm, consistent with the *FF* result shown in Fig. 3. By increasing the ETL thickness of cell B and C, lower ρ_c can be obtained. For the cells with same thickness of ETL, the contact resistivity of cell A is higher than cell B and cell C, which reveals that electrical properties of ITO / ETL interface can be improved by inserting nc-Si:H contact or seed layer. The contact resistivity of cell B and cell C are lower than reference cell when d_{ETL} of cell B and C is above 12 nm and 10 nm, respectively. Therefore, for cells with only 5 nm nc-SiO$_x$:H, similar electrical properties as reference cell can be achieved by inserting 7 nm nc-Si:H contact layer or 5 nm nc-Si:H seed layer on the front side. But for cell A with 20 nm nc-SiO$_x$:H, it still shows slightly higher

contact resistivity than reference cell.

To demonstrate scalability, we prepared bifacial cells on M2 wafer with three different cell types: i) cell A with 10 nm nc-SiO_x:H single layer, ii) cell B with double layer (5 nm nc-SiO_x:H and 5 nm nc-Si:H contact layer), and iii) cell C with double layer (5 nm nc-SiO_x:H and 5 nm nc-Si:H seed layer) as ETL. Table 2 shows that, for full-size cells with double layers (cell B and C), an increase of more than 3%$_{abs}$ of *FF* and 0.5%$_{abs}$ of η is demonstrated, compared with cell A. The best full-size cell, with introducing 5 nm contact layer, shows V_{oc} of 739 mV, *FF* of 80.7%, J_{sc} of 38.7 mA/cm^2 and efficiency of 23.1%.

Table 1

I-V parameters of full-size rear-junction SHJ solar cells with three different cell types: i) cell A with 10 nm nc-SiO_x:H single layer, ii) cell B with double layer (5 nm nc-SiO_x:H and 5 nm nc-Si:H contact layer), and iii) cell C with double layer (5 nm nc-SiO_x:H and 5 nm nc-Si:H seed layer) as electron transport layer (ETL). The cell structure is depicted in Fig. 1.

Cell type	J_{sc} (mA/cm^2)	V_{oc} (mV)	*FF* (%)	*pFF* (%)	η (%)
Cell A	39.2	740	77.2	84.7	22.4
Cell B	38.7	739	80.7	84.1	23.1
Cell C	38.6	738	80.3	84.6	22.9

3.2 Simulation results

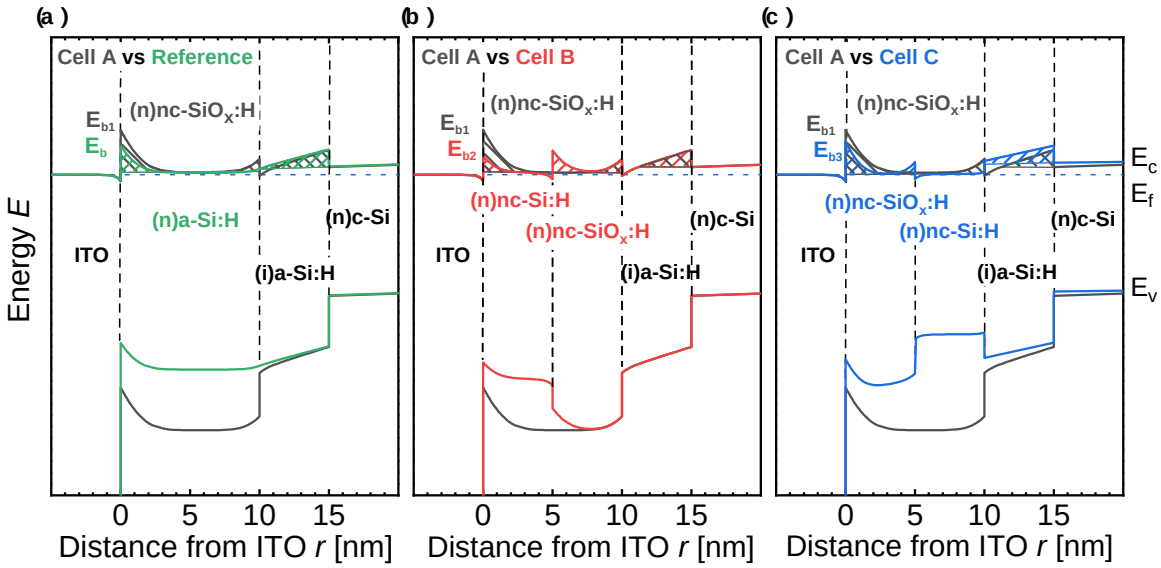

Fig. 8. Band diagram at equilibrium of 10 nm electron transport layer (ETL) of different SHJ solar cells, (a) cell A vs reference, (b) cell A vs cell B and (c) cell A vs cell C, calculated by simulator AFORS-HET. Cell A has an ETL consisting of nc-SiO_x:H single layer. Cell B is the cell type with nc-Si:H contact and nc-SiO_x:H layer.

Cell C is the cell type with nc-SiO_x:H and nc-Si:H seed layer. The cell with 10 nm (n) a-Si:H film was used as reference cell. E_c (E_v) and E_f are conduction (valence) band energy level and Quasi-Fermi level, respectively. The cell structures are depicted in Fig. 1.

Fig. 8 shows the band diagrams of three different kinds of SHJ solar cells (cell A, B and C) with 10 nm ETL at thermal equilibrium, simulated by AFORS-HET simulator. The input parameters of layers are listed in Table 2 [15,39,41]. The patterned areas in conduction band denote the energy barriers for electrons. They are defined by band offset at hetero-interface and inner band bending in doped layers. Fig. 8(a) shows a band offset on the heterointerface of (n) nc-SiO_x:H and (i) a-Si:H layers in cell A, which can't be found in reference cell. Furthermore, the band offset on the interface of ITO and n layer in cell A is higher than reference cell. These differences of the conduction band bending could be responsible to the lower *FF* and higher contact resistivity of the cells with 10 nm nc-SiO_x:H single layer, compared with reference cell (Fig. 3, Fig. 7).

Table 2

Input parameters of the layers for AFORS-HET simulator.

Parameter	ITO	nc-SiO_x:H (n)	nc-Si:H (n)	a-Si:H (n)	a-Si:H (i)	c-Si (n)	a-Si:H (p)
Thickness (nm)	70	10	10	10	5	170×10^3	8
Electron affinity (eV)	4.2	3.9-3.75	4.0	3.9	3.9	4.05	3.9
Mobility gap (eV)	2.8	1.8-2.1	1.4	1.72	1.72	1.12	1.72
Doping density (cm^{-3})	1×10^{20}	8×10^{19}	8×10^{19}	8×10^{19}	-	1.6×10^{15}	5×10^{19}
Electron (hole) mobility ($cm^2/V \cdot s$)	40 (20)	20 (5)	40 (10)	20 (5)	20 (5)	1335 (463)	20 (5)
Effective conduction (valence) band density	1×10^{20} (1×10^{20})	1×10^{20} (1×10^{20})	1×10^{20} (1×10^{20})	1×10^{20} (1×10^{20})	1×10^{20} (1×10^{20})	2.85×10^{19} (2.69×10^{19})	1×10^{20} (1×10^{20})
Layer density	2.328	2.328	2.328	2.328	2.328	2.328	2.328

The nc-SiO_x:H is a two-phase material with nanocrystalline silicon phase that has higher doping efficiency than a-Si:H, embedded in a highly transparent amorphous silicon oxide matrix [24-26]. During the deposition process of nc-SiO_x:H layer, a certain amorphous phase appears firstly as the nucleation of crystalline phase, then the epitaxial growth is followed [28-31]. Decreasing the thickness of nc-SiO_x:H layer leads to a layer with lower crystalline volume fraction, as shown in Fig. 7(a), and higher percentage of amorphous silicon oxide phase. When more oxygen incorporation in silicon film, higher average Si-Si bond energy in lattice

can be achieved [39]. The energy level of valence band edge may move down and conduction band edge come up in energy, giving rise to lower electron affinities (χ) of thinner nc-SiO_x:H [40]. Therefore, for cells with 5 nm nc-SiO_x:H layer the conduction band offset at ITO / nc-SiO_x:H interface might be higher than the cells with thicker nc-SiO_x:H layer and act as a Schottky barrier for the electrons, resulting in a lower FF and higher contact resistivity.

Compared with nc-SiO_x:H film, the electron affinity of nc-Si:H is higher [39, 41]. Fig. 8(b) shows the band diagrams of cell A with 10 nm nc-SiO_x:H single layer and cell B with 5 nm nc-Si:H contact layer and 5 nm nc-SiO_x:H layer. There is a band offset at nc-Si:H / nc-SiO_x:H interface in cell B, but it is lower than the band offset at ITO / nc-SiO_x:H interface in cell A. Furthermore, the band offset at ITO / ETL interface is reduced significantly by using ultra-thin nc-Si:H film as contact layer in cell B, consistent with the result in Fig. 7(b). Fig. 8(c) shows that the energy barrier can be reduced by using nc-Si:H underneath nc-SiO_x:H as a seed layer. The nc-SiO_x:H layer with higher crystalline volume fraction can be obtained at the same thickness of ETL when putting nc-Si:H underneath, as shown in Fig. 7(b) and Ref [33]. Therefore, the electron affinity of nc-SiO_x:H in cell C could be higher than it in cell A, which contributes to lower band offset at ITO / ETL interface as well as the energy barriers to the electron in cell C.

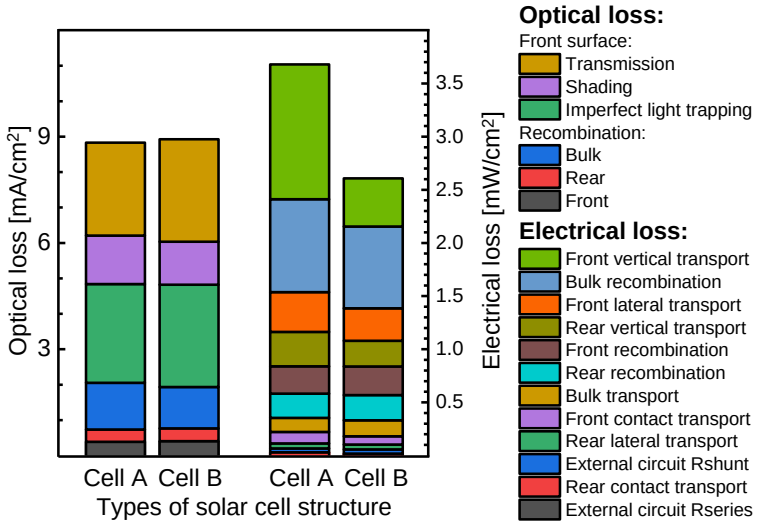

Fig. 9. Optical (left) and electrical (right) loss analysis for the full-size cells with different cell structure, Cell A (10nm nc-SiO_x:H single layer), Cell B (5 nm nc-SiO_x:H with 5 nm nc-Si:H contact layer), based on the 3D Quokka simulation. Note that the power loss scale in mW/cm^2 is equivalent to an efficiency loss in $\%_{abs}$.

Additionally, for full-size cells with 10 nm single layer and 10 nm double layer (5 nm

nc-SiO_x:H with 5 nm nc-Si:H contact layer), we built a cell model in Quokka 3 to quantify the optical and electrical losses [42]. Fig. 9 shows the optical (left) and electrical (right) loss analysis for the full-size cells with Smartwire (3% shading) and reveals that the main optical loss arise from the front imperfect light trapping for both solar cells, and the main electrical loss come from front vertical transport for cell A and from recombination within c-Si bulk for cell B. By replacing 10 nm nc-SiO_x:H single layer with 10 nm double layer (5 nm nc-SiO_x:H with 5 nm contact layer), the electrical loss relating to front vertical transport can be strongly reduced and the optical loss owing to front surface transmission increased slightly, which is consistent with the result mentioned previously.

4. Conclusion

In this work, the nanocrystalline silicon (nc-Si:H) contact or seed layer was introduced in solar cell with ultra-thin nc-SiO_x:H and the impact of the nc-Si:H thickness on the cell performance of rear-junction silicon heterojunction (SHJ) solar cells were investigated. For solar cells with nc-SiO_x:H layer, 20 nm nc-SiO_x:H is needed to guarantee the *FF*. The contact resistivity at ITO / n-layer interface plays an important role on the cell performance. For solar cells with ultra-thin (5 nm) nc-SiO_x:H layer, J_{sc} of 39.9 mA/cm^2 and similar iV_{oc} as reference cell can be obtained, but the contact resistivity at ITO / ETL interface is very high.

By inserting nc-Si:H contact or seed layer upon or underneath the nc-SiO_x:H layer and increasing the ETL thickness, higher crystalline ETL and lower front contact resistivity can be achieved. The best solar cell, with 5 nm nc-SiO_x:H and 5 nm nc-Si:H contact layer, exhibits V_{oc} of 726 mV, *FF* of 78.6%, J_{sc} of 39.6 mA/cm^2 and η of 22.6% at an aperture area of 19 × 19 mm^2. To demonstrate scalability, bifacial SHJ solar cells, with 10 nm nc-SiO_x:H single layer and 10 nm nc-Si:H / nc-SiO_x:H double layer, were fabricated on M2 size wafer. The cell performance of the solar cell with seed layer is similar as the solar cell with contact layer. For solar cells with 10 nm double layer, an increase of more than 3%$_{abs}$ of *FF* and 0.5%$_{abs}$ of η is demonstrated, compared with the solar cells with 10 nm nc-SiO_x:H layer. The η of 23.1% was obtained on M2 size by the solar cell with 5nm nc-SiO_x:H and 5nm nc-Si:H contact layer.

The front side energy band diagram of cells with three different 10 nm ETLs were simulated by AFORS-HET simulator. The result indicates that the energy barrier for electrons at

ITO / ETL interface can be reduced by inserting nc-Si:H layer upon or underneath the nc-SiO_x:H layer. Additionally, the solar cell simulator Quokka 3 was used to analyze the optical and electrical losses of those full-size cells. Compared with solar cells with 10nm nc-SiO_x:H single layer, we found a bit higher front surface transmission optical loss but much less front vertical transport electrical loss in solar cells with 10nm nc-Si:H / nc-SiO_x:H double layer.

Acknowledgment

The authors would like to thank Hildegard Siekmann, Alain Doumit, Iris Caspers, Andreas Mück, Silke Lynen, Andreas Schmalen, Johannes Wolff, Daniel Weigand and Wilfried Reetz for technical assistance. This work was supported by the Bundesministerium für Wirtscaft und Energie in the framework of the STREET project (grant: DB001618) and the HEMF (Helmholtz Energy Materials Foundry) infrastructure funded by the (HGF) Helmholtz association. The author is grateful for the financial support from China Scholarship Council (No. 201706380037).

References

[1] S. De Wolf, et al., High-efficiency silicon heterojunction solar cells: A review, Green. 2 (2012) 7–24.

[2] C. Ballif, et al., The amazing improvement of silicon hetero-junction technology: ready for a true mass market launch, WCPEC (2018) 2100–2103.

[3] https://www.pv-magazine.com/2019/11/20/hanergy-sets-new-heterojunction-module-efficiency-record/.

[4] M. Taguchi, et al., 24.7% Record efficiency HIT solar cell on thin silicon wafer, IEEE J. Photovolt. 4 (1) (2014) 96–99.

[5] D. Adachi, et al., Impact of carrier recombination on fill factor for large area heterojunction crystalline silicon solar cell with 25.1% efficiency, Appl. Phys. Lett. 107. 233506 (2015).

[6] K. Masuko, et al., Achievement of more than 25% conversion efficiency with crystalline silicon heterojunction solar cell, IEEE J. Photovolt. 4 (2014) 1433–1435.

[7] M. Bivour, et al., Rear Emitter Silicon Heterojunction Solar Cells: Fewer Restrictions on the Optoelectrical Properties of Front Side TCOs, Energy Procedia. 55 (2014) 229-234.

[8] J. Schmidt, et al., Surface passivation of crystalline silicon solar cells: Present and future, Sol. Energy Mater. Sol. Cells 187 (2018) 39-54.

[9] K. Yoshikawa, et al., Exceeding conversion efficiency of 26% by heterojunction interdigitated back contact solar cell with thin film Si technology, Sol. Energy Mater. Sol. Cells 173 (2017) 37–42.

[10] S.Y. Herasimenka, et al., >750 mV open circuit voltage measured on 50 μm thick silicon heterojunction solar cell, Appl. Phys. Lett. 103 (5) (2013) 053511.

[11] P. Balaji, et al., Development of 40 μm thin flexible silicon heterojunction solar cells, WCPEC (2018) 2100-2103.

[12] T. Kinoshita, et al, The Approaches for High Efficiency HIT Solar Cell with Very Thin (<100 μm) Silicon Wafer over 23%, EU PVSEC (2011) 871-874.

[13] Z. Holman, et al., Current losses at the front of silicon heterojunction solar cells, IEEE J. Photovolt. 2 (2012) 7–15.

[14] L. Mazzarella, et al., p-type microcrystalline silicon oxide emitter for silicon heterojunction solar cells allowing current densities above 40 mA/cm2, Appl. Phys. Lett. 106 (2) (2015) 023902.

[15] S. Kirner, et al., Silicon heterojunction solar cells with nanocrystalline silicon oxide emitter: Insights into charge carrier transport. IEEE J. Photovolt. 5(6) (2015) 1601-1605.

[16] L. Mazzarella, et al., Nanocrystalline n-Type silicon oxide front contacts for silicon heterojunction solar cells: photocurrent enhancement on planar and textured substrates, IEEE J. Photovolt. 8 (2017) 70-78.

[17] A. Richter, et al., Versatility of doped nanocrystalline silicon oxide for applications in silicon thin-film and heterojunction solar cells, Sol. Energy Mater. Sol. Cells 174 (2018) 196-201.

[18] A. Lambertz, et al., Microcrystalline silicon–oxygen alloys for application in silicon solar cells and modules, Sol. Energy Mater. Sol. Cells. 119 (2013) 134-143.

[19] A. Richter, et al., Light management in planar silicon heterojunction solar cells via nanocrystalline silicon oxide films and nano-imprint textures, physica status solidi (a). 213(7) (2016) 1976-1982.

[20] A. Richter, et al., Nano-composite microstructure model for the classification of hydrogenated nanocrystalline silicon oxide thin films, Surface and Coatings Technology. 295 (2016) 119-124.

[21] L. Mazzarella, et al., Ultrathin nanocrystalline n-type silicon oxide front contact layers for rear-emitter silicon heterojunction solar cells, Sol. Energy Mater. Sol. Cells 179 (2018) 386–391.

[22] Ding, Kaining, et al., Wide gap microcrystalline silicon oxide emitter for a-SiOx:H / c-Si heterojunction solar cells, Japanese Journal of Applied Physics 52.12R (2013) 122304.

[23] V. Smirnov, et al., Doped microcrystalline silicon oxide alloys for silicon-based photovoltaics: optoelectronic properties, chemical composition, and structure studied by advanced characterization techniques, Phys. Status Solidi 213 (2016) 1814–1820.

[24] M. Klingsporn, et al., Resolving the nanostructure of plasma-enhanced chemical vapor deposited nanocrystalline SiO_x layers for application in solar cells, J. Appl. Phys. 119 (2016) 223104.

[25] P. Cuony, et al., Silicon filaments in silicon oxide for next-generation photovoltaics, Adv. Mater. 24 (2012) 1182–1186.

[26] A.B. Morales-Vilches, et al., Nanocrystalline vs. Amorphous n-Type Silicon Front Surface Field Layers in Silicon Heterojunction Solar Cells: Role of Thickness and Oxygen Content, 33rd European Photovoltaic Solar Energy Conference and Exhibition, 2017, 715.

[27] O. Vetterl et al., Intrinsic microcrystalline silicon: A new material for photovoltaics, Sol. Energy Mater. Sol. Cells, 62 (2000) 97-108.

[28] B. Strahm, et al., Plasma silane concentration as a determining factor for the transition from amorphous to microcrystalline silicon in SiH4 / H2 discharges, Plasma Sources Sci. Technol., 16 (2007) 80-89.

[29] P. Roca i Cabarrocas, et al., Substrate selectivity in the formation of microcrystalline silicon: mechanisms and technological consequences, Appl. Phys. Lett. 66 (1995) 3609.

[30] P. Roca i Cabarrocas, et al., Microcrystalline silicon thin-films grown by plasma enhanced chemical vapour deposition-growth mechanisms and grain size control, Solid State Phenom. 93 (2003) 257-268.

[31] L. Mazzarella, et al., Nanocrystalline silicon oxide emitters for silicon hetero junction solar cells, Energy Procedia 77 (2015) 304-310.

[32] T. Watahiki, et al., Rear-emitter Si heterojunction solar cells with over 23% efficiency, Appl. Phys. Express 8 (2015) 21402.

[33] D. P. Pham, et al., Ultra-thin stack of n-type hydrogenated microcrystalline silicon and silicon oxide front contact layer for rear-emitter silicon heterojunction solar cells, Materials Science in Semiconductor Processing. 96 (2019) 1-7.

[34] R. Varache, et al., Investigation of Selective Junctions Using a Newly Developed Tunnel Current Model for Solar Cell Applications, Sol. Energy Mater. Sol. Cells 141 (2015) 14-23.

[35] R. Stangl, et al., General principles of solar cell simulation and introduction to AFORS-HET, Physics and Technology of Amorphous-Crystalline Heterostructure Silicon Solar Cells. Engineering Materials, vol 0. Springer, Berlin, Heidelberg (2012) 445-458.

[36] A. Fell, A free and fast three-dimensional / two-dimensional solar cell simulator featuring conductive boundary and quasi-neutrality approximations, IEEE Trans. Electron Devices. 60 (2) (2013) 733–738.

[37] A. Fell, et al., Input parameters for the simulation of silicon solar cells in 2014, IEEE J. Photovolt. 5 (4) (2015) 1250-1263.

[38] A. Fell, et al., The concept of skins for (silicon) solar cell modelling, Sol. Energy Mater. Sol. Cells 173 (2017) 128-133.

[39] R. Biron, et al., Window layer with p-doped silicon oxide for high Voc thin-film silicon n-i-p solar cells, Journal of applied physics. 110 (12) (2011) 124511.

[40] R. Carius, et al., Photoluminescence in the amorphous system SiOx, Journal of Applied Physics. 52 (6) (1981) 4241-4243.

[41] R. Biron, et al., Origin of the Voc enhancement with a p-doped nc-SiOx:H window layer in n-i-p solar cells, Journal of non-crystalline solids 358 (17) (2012) 1958-1961.

[42] R. Brendel, et al., Theory of analyzing free energy losses in solar cells, Appl. Phys. Lett. 93 (17) (2008) 173503.